Journal Name

Why are Zn-rich Zn-Mg nanoalloys optimal protective coatings against corrosion? A first-principles study of the initial stages of the oxidation process[†]

P. Álvarez-Zapatero,[*a] A. Lebon,[*b] R.H. Aguilera del Toro,[a] A. Aguado,[a] A. Vega[a]

ZnMg alloys of certain compositions in the Zn-rich side of the phase diagram are particularly efficient, and widely used, as anticorrosive coatings, but a sound understanding of the physico-chemical properties behind such quality is still far from being achieved. The present work focuses on the first stage of the corrosion process, namely the initial growth of a sacrificial surface oxide layer, whose characteristics will condition the next stages of the corrosion. A comprehensive *ab-initio* study, based on the density functional theory, is carried out on ZnMg nanoalloys with 20 atoms and different compositions, which serve as model systems to simulate the complex processes that occur in extended granular surfaces. The structural and electronic properties, when progressive oxidation of the nanoalloys takes place, are analyzed in detail with the help of structural descriptors, energetic descriptors such as the oxygen adsorption energies and excess adsorption energies, as well as with electronic ones based on the topological analysis of the electron density and the electron localization function, from which a detailed analysis of the bonding patterns is extracted. We explain why small amounts of Mg create a very positive synergy between Zn and Mg that increases the reactivity to oxygen while reducing, at the same time, the stress induced on the cluster substrate, both facts working in favor of promoting the growth of the oxide crust whilst protecting the core. Moreover, we also show that stoichiometries close to the Mg_2Zn_{11} and $MgZn_2$ compositions are the best candidates to optimize the protection against corrosion in Zn-Mg alloys, in agreement with the experimental observations.

1 Introduction

The use of protective coatings containing zinc[1] is a general practice in automotive, building, and other industries to extend the lifetime and appearance of products. Zinc-magnesium alloys with low magnesium content have been shown to provide very good protective coating properties that even outperform those of pure zinc. For instance, corrosion tests in automotive laboratories[2] have shown that the time for growing significant amounts of red rust under spraying with NaCl is three times longer when applying coatings consisting of a $MgZn_2$ alloy than if pure Zn coatings are employed. The pH dependence in an aqueous NaCl solution environment has been thoroughly investigated[3]. Protection against oxidation was also investigated, the optimal magnesium content in the coating being 4-8 wt.%; for this particular alloy, the

weight loss is up to 10 times lower than that measured for pure Zn[4]. The microstructure and the possible multilayer arrangement of Zn-Zn/Mg has been also carefully investigated[5] since the coating properties do not only depend on the resistance to a corroding agent but also on the microstructure of the protective layers. The influence of macrosegregation, microstructure evolution and microstructure length scale on the corrosion properties of a Zn-5.0wt.%Mg alloy casting were also analyzed[6]. Finally, the corrosion problem is a very general subject that is not limited to Zn or Zn-Mg systems. For instance, an *ab-initio* study was performed on Fe-Cr alloy surfaces in order to analyse at an atomic level the initial oxidation stages in these surfaces[7], in a similar way as we shall show in this work.

For a given protective coating under particular external conditions, the corrosion process is quite complex, involving physical, chemical, thermodynamical and kinetic mechanisms, as well as several stages that are yet far from being completely understood in the time scale. It is known, for instance, that the improved anticorrosive properties of $MgZn_2$, derived from the decrease of the charge transfer across the interface as compared to pure Zn coatings, are a consequence of the different proportion of hydrox-

[a] *Departamento de Física Teórica, Atómica, y Óptica. Universidad de Valladolid, E-47011 Valladolid, Spain. E-mail: pablo.alvarez.zapatero@uva.es*
[b] *Laboratoire de Chimie Électrochimie Moléculaire et Chimie Analytique, UEB/UBO, UMR CNRS 6521, 29238 Brest Cedex, France. E-mail: alexandre.lebon@univ-brest.fr*

ide and carbonate species in the final corrosion products, which increase the work function of the surface[8]. It is also known[9] that the thickness of the corrosion film of the ZnMg coating is thicker than that of a pure Zn coating, which favors passivation of the surface in a chloride-rich atmosphere due to the lowering in the gradient of the electrostatic potential across the metal-oxide interface. In the first stage of the corrosion process, the formation of an oxide surface layer is observed[4].The improved coating properties of Zn-Mg alloys are closely connected with the superior capability of Mg atoms to promote the protective surface oxide layer, being more stable than the oxide surface that pure Zn would form. Oxygen preferentially binds to Mg and even favors Mg enrichment at the surface, which produces an oxide surface layer with more Mg concentration than the nominal concentration in the alloy.

The physical and chemical mechanisms that determine the corrosion process along the different stages are triggered by fundamental structural and electronic properties of the system which are difficult to understand in depth without a quantum-mechanical analysis. For example, the granularity that characterizes usual protective coatings can decisively modify their properties[10]. The microstructure of the coating must also be considered with special care, since penetration and fast diffusion of the corroding agents are easier through local defects.

In previous works[11–13], we have reported first-principles calculations for ZnMg *in vacuum* nanoalloys of several sizes and composition ratios, to obtain hints into the fundamental physico-chemical properties that might ultimately explain the reasons for the improved capability of ZnMg coatings against corrosion. A noticeable charge transfer from Mg to Zn atoms was identified and rationalized, modulated by composition-dependent features. We also showed that Mg atoms are more reactive than Zn atoms, so that the oxidation of the nanoalloy surface is a faster and more exothermic process as compared to oxidation of pure, all those facts being consistent with the experimental evidences. The results of these initial works also allowed us to generate a significant number of accurate nanoalloy structural models as an input for the explicit corrosion studies, and to determine fundamental indicators that point to certain Zn-Mg compositions as the optimal ones for protective coatings.

The present work, on the contrary, focuses on the first stage of the corrosion process, that is the formation of an oxide surface layer and related structural and electronic properties that can be relevant for the next stages of the corrosion process. For this purpose, ZnMg nanoalloys of 20 atoms have been chosen, for which the reactivity indicators were analyzed in detail in our initial work[11]. We have investigated, at a first-principles level, both the molecular and dissociative adsorptions of O_2 for several compositions. The results allow to better understand now why certain compositions are better suited to the design of optimal protective ZnMg coatings, taking into account that the characteristics of the formed oxide surface layer will condition the next stages of the process.

Small nanoalloy clusters are used in this work since these are simple yet useful computational models for an initial study of the intricate processes that operate in the real extended surfaces. A perfectly periodic slab model would not necessarily be closer to the realistic situation, because the real materials are granular in nature and the defects or cracks associated with the microstructure of the sample have been found to be essential for corrosion, as explained above. Thus, the local features of the surface play a critical role in the overall corrosion process[14–16]. Additionally, it is relevant in our opinion to study nanoclusters as most coating techniques involve sputtering or spray methods where the material could be fragmented through surface-induced dissociation as expected in physical vapour deposition technology[4], either while hitting the surface or by collision of powder crystallites during the deposition process. In such a case, the beginning of oxidation could occur in regions of nanometer size that are expected to be formed around cracks and that are ill-measured by electronic microscopy techniques. It is worth emphasizing that nanoalloys offer the possibility to simulate the variety of local environments that appear in real granular surfaces, and as will be shown in this paper, corrosion/oxidation processes are ultimately related to the local reactivity. Finally, in one of our recent studies[13], we have obtained the global minimum structures of $(MgZn_2)_N$ nanoalloys of varying sizes, and compared them to the bulk Laves structure. That study demonstrates that the nanoalloys look very similar to the bulk material as regards the short-range skeletal and compositional orders, which adds to our idea that the nanoalloys are good model systems, representative of extended samples at least locally, but additionally displaying a larger variety of similar environments as expected in a granular sample. The only significant size effect is that bond lengths are homogeneously scaled down in nanoalloys as compared to the bulk limit (this is generally true for nearly all metallic nanoparticles). We will discuss the expected size effects on the oxidation process, and argue that they do not fundamentally alter the identified mechanisms.

The theoretical approach, based on the density functional theory, is first detailed in the next section. Then the putative ground state configurations are analyzed with the use of structural and energetic descriptors together with indicators deduced from a quantum chemical topology analysis. The selected nanoalloys, Zn_xMg_{20-x} with $x = 0, 10, 13, 15, 17, 20$, are subjected to a progressive oxidation with the addition of up to 6 oxygen atoms. The Mg content is low for the majority of the analyzed stoichiometries, which were selected on the basis of the experimental results that demonstrate that the best coating properties are found for Zn-rich alloys. On the other hand, the $x = 17$ and $x = 13$ stoichiometries are in the range that mimics the alloys at 4-8 wt % for the former and the $MgZn_2$ for the latter.

2 Theoretical and Computational Methods

Ground state (GS) configurations (both atomic structure and chemical order) of the bare Zn_xMg_{20-x} nanoalloys were taken from a previous work[11]. Density Functional Theory calculations of molecular and dissociative O_2 adsorption on all non equivalent surface sites of those nanoalloys have been performed employing the code VASP[17,18]. Electron-ion interactions are described with the projector-augmented-wave (PAW) potentials available within VASP code. Exchange and correlation effects were described with the generalized gradient approximation of Perdew,

Burke and Ernzerhof (PBE)[19]. This functional was found to provide accurate enough results regarding the structural, energetic and elastic properties of zinc and magnesium oxides[20–22], which are the essential properties we need in our discussion. A hybrid functional would be needed, however, to describe some properties of the electronic density of states, as for example the HOMO-LUMO gap, which for metal oxides are not properly captured by semilocal functionals. An energy cutoff of 500 eV was used for the plane wave basis set. The tolerance for the electronic density in the selfconsistent calculation was set at 10^{-4}. We checked all our calculations for spin polarization, and found that all GS configurations are in a singlet spin state.

Each calculated cluster is placed in a $30 \times 30 \times 30$ Å^3 supercell. The calculations include only the Γ point as appropriate for finite size systems. The structure is optimized by relaxing the atomic positions until the force on each atom is smaller than 0.01 eV/Å.

Local atomic populations were derived with the Bader's method[23] following the algorithm of Henkelman[24]. To analyze the changes in local reactivity of the Zn-Mg system upon O$_2$ adsorption, the Fukui f^+ and f^- [25–27] functions have been computed. The Fukui functions can be presented either as isosurface (contour) plots or in its condensed form which is obtained by integrating them over the Bader atomic basins[25]. Further details can also be obtained from our previous work[11]. Following the common practice of approximating the derivatives by finite differences, the expressions for a cluster with N_e electrons are:

$$f_{N_e}^+(\vec{r}) = \rho_{N_e+1}(\vec{r}) - \rho_{N_e}(\vec{r}) \qquad (1)$$

$$f_{N_e}^-(\vec{r}) = \rho_{N_e}(\vec{r}) - \rho_{N_e-1}(\vec{r}) \qquad (2)$$

The corrosion process is accompanied with drastic changes in the structure and energetics of the clusters. To determine how the stability changes when Zn$_x$Mg$_{20-x}$ clusters are exposed to oxidation, two excess energy indicators have been defined. The first one is the standard excess energy definition, adapted to deal with partially oxidized metals:

$$E_{exc}(\text{Zn}_x\text{Mg}_{20-x}\text{O}_m) =$$
$$= E(\text{Zn}_x\text{Mg}_{20-x}\text{O}_m) - x\frac{E(\text{Zn}_{20}\text{O}_m)}{20} - (20-x)\frac{E(\text{Mg}_{20}\text{O}_m)}{20}, \qquad (3)$$

where $E(\text{Zn}_{20}\text{O}_m)$ and $E(\text{Mg}_{20}\text{O}_m)$ are the energies of the oxidized Mg$_{20}$ and Zn$_{20}$ clusters. This definition reduces to the excess energy of Zn-Mg nanoalloys when $m = 0$. For $m \neq 0$, it quantifies how much favorable it is the formation of the oxidized nanoalloy as compared to an ideal mixture of oxidized Zn and oxidized Mg clusters of the same size. Next, we use the oxygen adsorption energies:

$$E_{ads}(\text{Zn}_x\text{Mg}_{20-x}\text{O}_m) =$$
$$= \left[\frac{1}{2}E(\text{O}_2) + E(\text{Zn}_x\text{Mg}_{20-x}\text{O}_{m-1})\right] - E(\text{Zn}_x\text{Mg}_{20-x}\text{O}_m), \qquad (4)$$

to define an excess adsorption energy:

$$E_{exc-ads}(\text{Zn}_x\text{Mg}_{20-x}\text{O}_m) =$$
$$= E_{ads}(\text{Zn}_x\text{Mg}_{20-x}\text{O}_m) - x\frac{E_{ads}(\text{Zn}_{20}\text{O}_m)}{20} - (20-x)\frac{E_{ads}(\text{Mg}_{20}\text{O}_m)}{20}, \qquad (5)$$

When positive, this excess energy demonstrates that oxygen adsorption is more exothermic in the oxidized nanoalloy than in a statistical mixture of the separately oxidized Mg and Zn metals. Its dependence with m determines how the oxygen content influences the adsorption energetics of additional oxygen atoms.

The progressive oxidation of the Zn$_x$Mg$_{20-x}$ nanoalloys is examined through a topological analysis of the electron density (ρ) and electron localisation function (ELF)[28] scalar fields. Regarding the electronic density, the examination of its critical points unveils the character of bonding[23]. The analysis of electron density gradients reveals maximal density lines connecting two atoms, and the minimum along this line is called a bond critical point (BCP). Several indicators are then determined at the BCPs, such as the value of the electronic density ρ_b, its Laplacian $\nabla^2\rho_b$, and the total electronic energy density H_b, which together make it possible to identify the nature of the bonding interaction[29–31]. The different types of bonds, according to Matta's classification[32], range between electron-sharing bonds and closed-shell interactions. All the data at the BCPs are provided in atomic units.

The ELF quantifies the amount of Pauli repulsion at each point of the molecular space[28,33], which is partitioned into bonding, non bonding and core basins. The latter reproduce the atomic core shell structures and are labeled by C(X) for an atom X. The valence basins (either bonding or non bonding) are classified according to their degree of synapticity. A disynaptic basin is a basin common to two atoms A and B, and is labeled as V(A,B). Non bonding basins are called monosynaptic since they are localized around a single A atom, and they are noted as V(A). They tipically correspond to lone pairs. The average population of each basin is derived after integrating the electronic density within the basin volume, and the population variance is similarly obtained from integration of the pair density.

In this study the optimized VASP structures served as input for single point calculations with the well-established quantum chemistry code Gaussian16[34]. These are motivated by the fact that the PAW-generated ELF and ρ display spurious minima around the cut-off radius[35]. As a consequence, compared to an all-electron calculation, there are differences in the building of the electron density or the ELF function. All Gaussian16 calculations are done at the same level of theory as the VASP calculations, employing a 6-311g(d) basis set. The gradient of the electron localization function (ELF) and the electronic density were computed with the codes TOPMOD09[36] and DGRID5.1[37].

3 Results and Discussion

3.1 Structural trends along the initial oxidation path

In a previous study, the GS structures of Zn$_x$Mg$_{20-x}$ nanoalloys were determined through self-consistent DFT calculations, with the same considerations and methodology as here. Global and

local reactivity descriptors were determined to inquire about the reactivity of the bare cluster[11]. Here, we have started with those GS configurations for the bare nanoalloys, that correspond to $Zn_xMg_{20-x}O_m$ for $m = 0$.
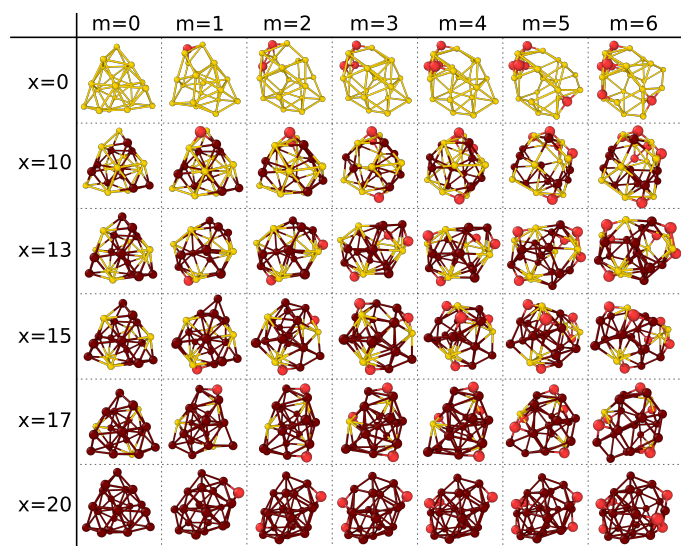

Fig. 1 Putative GS structures of $Zn_xMg_{20-x}O_m$ for $m = 0 - 6$, and $x = 0, 10, 13, 15, 17$ and 20. Brown, yellow and red spheres represent Zn, Mg and O atoms, respectively.

The putative GS structures of the oxidized and non-oxidized nanoalloys $Zn_xMg_{20-x}O_m$ (with $m = 0 - 6$ and $x = 0, 10, 13, 15, 17, 20$) are shown in Fig. 1. Our first relevant comment is that molecular chemisorption of O_2 is not even a stable local minimum in most cases, i.e. the molecule readily dissociates during the optimization process, demonstrating that, if an activation barrier exists for the dissociation process, it must be negligibly small. Only in very few runs could we obtain a local minimum with a chemisorbed O_2 molecule, and all those configurations were between 3 and 4 eV less stable than the correct GS structure. Once it was clear that only dissociative chemisorption is relevant in these systems, the GS structures for the oxidized nanoalloys were located by trying various initial locations for each additional adsorbed oxygen atom, including "hollow", bridge and atop positions over the cluster surface. The hollow sites correspond to the center of the triangular facets where the oxygen is bonded to three metal atoms, and are always the most stable adsorption sites. When other sites like bridge or atop positions were tested, either the calculation converged to a hollow site after relaxation, or the final relaxed structure was a highly excited isomer at more than 2 eV with respect to the GS. After having relaxed all the candidates with a single O atom, the most stable configuration was chosen as the new starting point to locate the optimal adsorption site for the second oxygen atom, and so forth. This search strategy was initially guided by calculations of the nucleophilic condensed Fukui functions f^-, performed on each $Zn_xMg_{20-x}O_m$ nanoalloy right before addition of the next oxygen atom (see Fig. S1 in the ESI). Considering that large f^- values are related to the propensity of an atomic site to experience an electrophilic attack, the initial position for the O atom

was proposed in the vicinity of those regions with higher f^-. However, with increasing oxygen content, we observed that the electrophilic attack can preferentially occur at other sites, i.e. f^- itself is not sufficient to unambiguously predict the adsorbed site of the additional oxygen atoms. The oxygen atom rather goes to a surface site where the bonding interactions with magnesium are maximized. For given values of oxygen content and nanoalloy composition, approximately 30 different adsorption configurations were tested, including those based on the largest f^- sites and those close to Mg-rich surface regions.

By adding the oxygen atoms one at a time and varying just the position of the newly added atom, we are obviously constraining the number of sampled configurations. When m oxygen atoms are added on top of a given nanoalloy structure (with a given atomic skeleton and chemical order), and if there are N_s hollow surface sites available on the substrate, a total of $\binom{N_s}{m}$ different configurations exist in principle for the oxidized system, which may be too many to try them all explicitly. Therefore, we can not claim to have located the absolute global minimum structure for m oxygen atoms on the surface of a Zn-Mg nanoalloy. On the other hand, we have performed additional optimizations for the $m = 2$ case not using that assumption (i.e. varying the possible adsorption sites of the two oxygen atoms) and have not located a more stable structure than when fixing the position of the first adsorbed oxygen. These additional tests justify our assumption and make us confident that the main structural trends have been correctly identified, i.e. that the obtained structures are representative of the true situation, even if there may be similar structures which are slightly more stable.

This dedicated procedure enabled us to finally obtain a bench of 42 putative GS structures that is representative of the initial oxidation scenario expected for these systems in the thermodynamic equilibrium limit corresponding to a low oxidation rate, because we are assuming that each oxygen atom reaches its most stable adsorption site before the next oxygen atom is added. To provide explicit support for our assumption, we have calculated the diffusion barriers of an oxygen adatom over the surface using the Nudged Elastic Band method[38,39] (see Fig. 2). In order to move between two neighboring triangular facets on the cluster substrate, an oxygen atom has to surmount a barrier which is between 0.3-0.6 eV. As we will later show, these barriers are between 5 to 10 times smaller than the oxygen adsorption energy, so right after adsorbing each oxygen atom, the cluster has enough internal energy for the oxygen atom to surmount the diffusion barriers before the excess heat is dissipated.

We first describe the main structural trends that can be extracted from a detailed visual inspection of the GS structures (Fig. 1), including a comparison with the initial oxidation stage in sodium clusters, that was analyzed in previous reports[40,41]. There are some systematic differences between the initial oxidation behaviors of Na, Mg, Zn and Zn-Mg systems that can be correlated with their specific structural properties. In sodium clusters, to start with, the oxygen atoms get absorbed at octahedral interstices that exist within the subsurface layer of the metal host, and when several oxygen atoms are added, they prefer to occupy neighboring interstices, thus generating a single sodium oxide
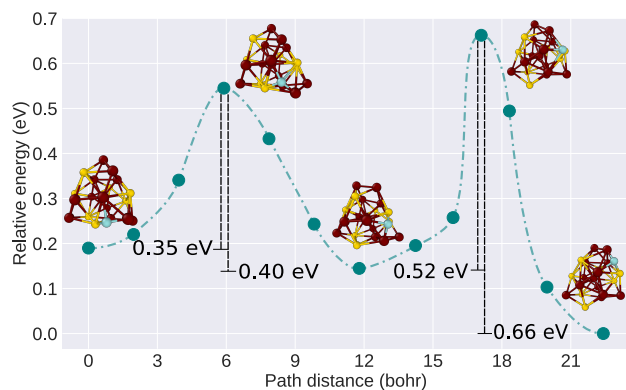
Fig. 2 Diffusion path analyzed for the oxygen atom in the $Zn_{13}Mg_7$ composition. The diffusion path comprises two different barriers, where the oxygen atom moves from a hollow position to another one, almost 4.5 Å away. Reddish colors represent Zn atoms, golden colors depict Mg atoms while oxygen atom is depicted in blue color. For the first barrier, the same elastic constant was employed for all the images, while for the second barrier a $k_{max}=2k_{min}$ scheme was used, in order to increase the resolution around the saddle point. Also the atomic configurations are shown for maximum and minimum energy values along the path.

sub-cluster well segregated from the metallic host[40,41]. The static coexistence of oxidized and metallic phases separated by an interface is in line with the bulk behavior[42]. Similarly, Na clusters are not able to dissolve the oxide molecule because the elastic deformation energy of the metal host when the oxygen impurities are dissolved is bigger than the energy cost of the interface. Purely steric factors finally explain the preference for subsurface sites: with an average interatomic distance of about 3.7Å, the octahedral interstices in sodium clusters have just the appropriate size to house an oxygen impurity without disrupting the whole cluster structure. Nevertheless, the oxidized region locally contracts, and puts the metallic host under a tensile stress which can not be fully compensated by elastic deformation mechanisms. Obviously a metal like sodium would be useless for corrosion protection as the oxide nucleation centers grow inside the metallic host right from the start, thus getting easy access to attack the core region.

The initial oxidation of Mg_{20} shares many similarities with the sodium case. In effect, the initial oxygen adatoms tend to be close to each other on the surface of the pure Mg_{20} cluster, thus preferentially attacking a specific local region of the cluster surface and inducing strong distortions in the structure of the metal host. As an example of these distortions, we observe that some oxygen atoms become coordinated to four metal atoms, while the shell of the pristine Mg_{20} cluster is well triangulated and only three metal-oxygen bonds would be expected if distortions were small (in other words, the initial hollow sites are not structurally stable). At the highest oxygen content here considered ($m = 6$), the local shrinking around the oxidized region puts the shell under a high tensile stress so the metallic bonds at the surface have significantly weakened; in order to alleviate the tension, some structural defects are created in the cluster shell, in the form of large square or even pentagonal "windows" through which additional oxygen atoms might penetrate inside the cluster core. Opposite to

sodium clusters, however, the average Mg-Mg distance in the pure cluster is about 3.1Å, the inner interstices are much smaller than in sodium, and the oxygen atoms prefer to be adsorbed rather than absorbed. Nevertheless, some oxygen atoms sit in an "in-plane" position within the shell, i.e. they are at a borderline separating adsorption from absorption. Thus, although the scenario is slightly more favorable due to steric factors, pure magnesium does not seem able to restrain the oxide from eventually percolating towards the interior of the metal, and it should be useless as a corrosion-protecting coating as well. The whole scenario is qualitatively identical in the equiatomic nanoalloy ($x = 10$), which suggests that all Mg-rich Zn-Mg alloys should be discarded in corrosion protection applications, in agreement with the experimental observations.

The initial oxidation stage is qualitatively different in Zn_{20}, which is much more efficient in dissolving the oxide impurities. In effect, the initial oxygen impurities adsorb at well separated surface sites, and at the highest oxygen content ($m = 6$) two separate oxide islands have formed on the cluster surface. With an average Zn-Zn distance of about 2.7Å, the oxidized region locally expands instead of shrinking as in the Mg case. All of the oxygen atoms get adsorbed at sites which are completely external to the metal shell, and thus more separated from the cluster core in a natural way because of purely steric factors. The number of structural defects in the cluster shell is much smaller than in Mg or Mg-rich clusters, suggesting that the tension stored in the metallic bonds is not so high as in Mg-based materials. The square or pentagonal defects are not only less abundant, but also significantly less reactive, as they never become the preferred adsorption site, while they were readily occupied by oxygen in Mg-rich alloys. In fact, when an oxygen atom is adsorbed on top of a square defect, the oxygen seals the aperture during optimization and ends up bonded to only three Zn atoms, thus naturally preventing the oxygen from approaching the cluster core. Thus, our calculations provide support and theoretical interpretation for the experimental observations of Zn being better suited than Mg as a sacrificial metal for corrosion protection applications.

Finally, the oxidation scenario is even better, and close to optimal, in Zn-rich nanoalloys. It is convenient to emphasize here that the functional material in real applications is the fully oxidized surface layer, i.e. it is the oxide crust formed on the surface that provides protection against corroding agents; but during the initial oxidation stages analyzed in this paper, it is the metal surface that must protect the core until the oxide crust is fully formed and, at the same time, it must strongly react with oxygen so that the oxide crust forms as soon as possible. A small amount of Mg added into Zn makes the initial oxidation reaction more exothermic (because oxygen atoms preferentially attach to Mg atoms), without increasing significantly the volume of the subsurface interstices or the average interatomic distances, both factors contributing to a more efficient oxidation of just the cluster shell, as the oxygen adatoms occupy clearly external positions. Additionally, and as shown in our previous works[12,13], Mg atoms tend to segregate to the surface of ZnMg nanoalloys due to their bigger atomic size, i.e. there is a slight Mg-enrichment of the shell in the nanoalloys, and this is another factor favoring shell oxidation

as compared to core oxidation. At the same time, the nanoalloys are maximally mixed on the cluster shell, so the number of Mg-Mg bonds is minimized and the number of the strongest Mg-Zn bonds is maximized. Therefore, at low Mg concentrations, Mg atoms occupy well separated and highly-coordinated surface sites. In the initial stages of oxidation, those Mg atoms in the shell act as attractors that anchor the oxygen adatoms, creating several nucleation centers evenly distributed across the cluster surface. The initial growth of the oxide phase thus displays a multi-center nature and evenly affects the whole surface, instead of concentrating into a single local region of the surface. This is expected to result in a much more uniform distribution of stress across the metal surface. Finally, the Mg atoms guide the oxygen atoms precisely towards those local regions in the surface that contain the strongest Zn-Mg metallic bonds, which are expected to be the most resistant ones at a structural level. Any square or pentagonal defects in the shell occur in Zn-rich regions so the Mg atoms also protect those defects from being attacked by oxygen in the initial stages of oxidation. All of these properties seem to conspire precisely to promote the growth of the oxide crust whilst protecting the core, an example of a very positive synergy between Zn and Mg for this particular application. As an example, the optimal composition here seems to be $x = 17$: for $m = 3$ there is one oxygen close to each Mg atom in the shell, for $m = 6$ two oxygen atoms bonded to each Mg. Thus it seems that the three islands grow independently and at the same rate. The only potential problem with this multi-center growth can occur during the last stages of oxidation, not covered yet in the present study. Some line defects might be generated at the interface where two independent oxide islands meet. We will consider this problem in future works, but for the time being our results suggest that some mild annealing post-processing treatment of the material might be beneficial for the microstructure of the oxide crust.

In what follows, we analyze several energetic, structural, and electronic indicators to provide a more quantitative support for our claims in the previous paragraphs. In Fig. 3 we plot the cumulative adsorption energies, representing the energy gain upon adsorption of m oxygen atoms on the bare cluster, against the number of metal-oxygen X-O bonds (with X=Mg or Zn). The non-cumulative adsorption energies are separately shown in the ESI. The number of bonds is ascertained by the existence of a BCP in between two nuclei, as explained in the previous section. A multivariate fitting on the whole set of data (as shown in the upper part of the figure) shows that the average energy gain upon formation of a Mg-O bond (1.17 eV/bond) is superior to the corresponding gain in the formation of a Zn-O bond (0.62 eV/bond). This accounts for the observation that the atom with the highest f^- value is not necessarily the best site for O adsorption in these systems. A supplementary condition must be fulfilled regarding the local chemical environment, specifically it must contain Mg atoms. Because of this preferential formation of Mg-O bonds, the excess adsorption energies (not shown explicitly) are positive for all nanoalloys (the curve for $Zn_{15}Mg_5$, for example, is closer to the pure Mg curve than to the pure Zn curve in Fig. 3, despite being a Zn-rich nanoalloy). Additionally, all of the cumulative adsorption energies display a slightly positive curvature, so
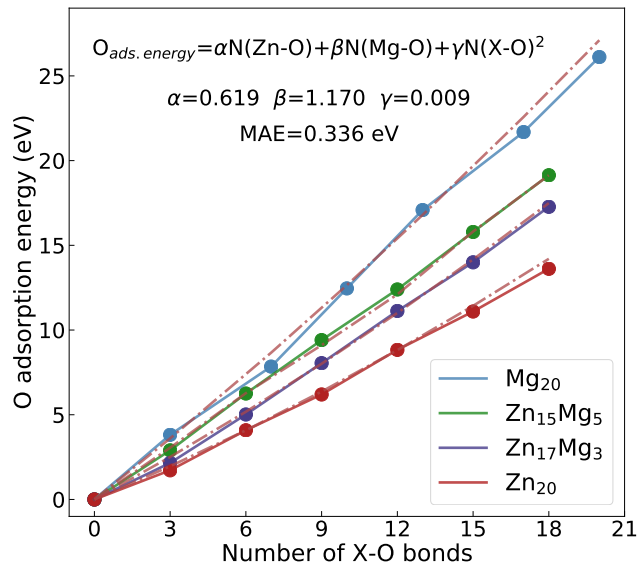

Fig. 3 Cumulative adsorption energies as a function of the number of metal-oxygen X-O bonds (X=Zn or Mg) for the pure clusters and some representative nanoalloys. The discontinuous red lines are the result of a multivariate fitting in terms of Zn-O, Mg-O and X-O bonds, performed on the whole set of data as shown in the upper insert. The mean absolute error (MAE) of the fit is also shown.

that oxygen adsorption becomes a more exothermic process the larger the oxygen content (see Fig. S2 in the ESI), and the oxide phase grows at an accelerated rate at least during its initial growth stage. Therefore, the structural changes induced by oxygen attachment weaken the metal-metal bonds and increase the reactivity of the metallic part.

Notice that, despite the difference of energy gain in forming a Mg-O bond with respect to a Zn-O bond, the average Mg-O and Zn-O interatomic distances are very much the same, since for all values of the oxygen content m both bonds are measured at $\approx$ 1.95 Å. Among the investigated metallic compositions, some of them display almost equal Zn-O and Mg-O distances irrespective of the number of adsorbed oxygen atoms, in particular $Zn_{17}Mg_3$ and $Zn_{13}Mg_7$. The similarity of these distances is consistent with the systematic placement in hollow sites of the adsorbed oxygen atoms, and with the fact that the larger atomic radius of Mg ($\approx$ 1.50 Å) as compared to Zn ($\approx$ 1.35 Å) is compensated by the stronger Mg-O interaction. The nearly constant metal-oxygen distances can be contrasted with significant variations observed in the Zn-Zn, Mg-Mg or Zn-Mg bond distances. As metal-oxide bonds are approximately 5 times stiffer than metal-metal bonds, the elastic deformation energy is dominantly stored in the metal phase. The Zn-Mg skeleton of the nanoalloys is, therefore, withstanding the deformation generated by the adsorption of oxygen atoms.

Table 1 lists the number of Mg-O and Zn-O bonds for the whole set of nanoalloys investigated, as these are not easily appreciated from a visual inspection of Fig. 1. Once again we stress the fact

that the number of bonds has been unambiguously determined within the QTAIM theoretical approach instead of just counting neighbors within a given cutoff distance. Table 1 confirms that the oxygen atoms generally sit on positions where one O atom is bonded to three atoms, but exceptions to this rule occur in the pure Mg cluster and also in the $Zn_{10}Mg_{10}$ nanoalloy, where some of the O atoms bind to four metal atoms. These exceptions can only be explained by a more important surface reconstruction upon oxygen adsorption, or a higher reactivity of square rings, in Mg-rich nanoalloys, confirming our previous claims. Concerning Zn-rich nanosystems, we observe some regularities for compositions $x = 13$ and $x = 17$: in the $Zn_{17}Mg_3$ nanoalloy, oxygen adsorption occurs on top of a $MgZn_2$ triangular hollow site as these are the only Mg-containing facets at such a low Mg concentration; in $Zn_{13}Mg_7$, however, the oxygen preferentially attach to Mg_2Zn triangles as long as they are available. In summary, these trends demonstrate that oxygen atoms would fill the available hollow triangular sites in the following order: Mg_3, Mg_2Zn, $MgZn_2$ and finally Zn_3 triangles. As all the nanoalloys with $x \geq 10$ are well mixed [12], there are no Mg_3 facets naturally occurring on their surfaces. Nevertheless, Table 1 shows that some oxygen atoms attach to three Mg atoms for the $x = 10$ composition, demonstrating that the presence of oxygen induces segregation of Mg atoms towards a local region of the shell.

Fig. 4 displays the excess energy of the oxidized and non-oxidized nanoalloys according to eq. 3. For oxygen-free alloys, we know from previous works [11] that $x = 10$ is the most stable composition, because it contains the largest possible number of the strongest Zn-Mg metallic bonds. This figure now confirms that alloying of the oxidized metals is a more exothermic process than the alloying of the pure metals, and more so the larger the oxygen content. The reason for this behavior is apparent from the results in Fig. 3, that demonstrate a positive oxygen adsorption excess energy: as compared to an ideal statistical mixture of the oxidized metals (governed by Vegard's law), the oxidized nanoalloy is much more stable because the number of the strongest Mg-O bonds is larger than in the statistical mixture.
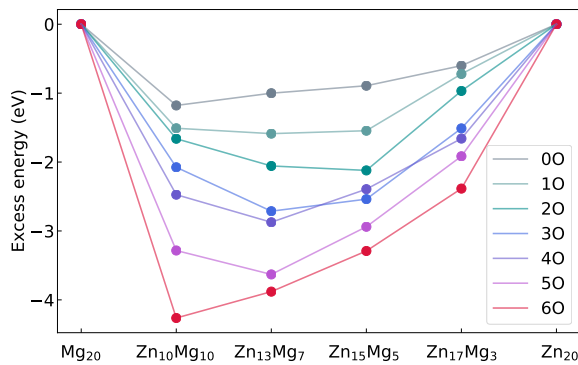

Fig. 4 Excess energy of $Zn_xMg_{20-x}O_m$ nanoalloys, for all different oxygen contents.

In order to quantify the global structural changes undergone by the metallic skeleton upon oxygen adsorption, we first analyze the evolution of its volume and its shape as a function of oxygen content. Fig. 5 displays the volume of the inertia ellipsoid and the Hill-Wheeler asphericity parameter β [43,44], which is obtained from the principal moments of inertia $I_1 \geq I_2 \geq I_3$ (evaluated with all the atomic masses set to unity) as:

$$I_k = \frac{2}{3}r^2\left(1 + \beta\sin(\gamma + \frac{(4k-3)\pi}{6})\right), \qquad (6)$$

where $r = (I_1 + I_2 + I_3)/2$ is a measure of the average cluster radius. β quantifies the quadrupole shape deformation, and γ (not shown explicitly) determines if that deformation is prolate or oblate. The maximum value of β is 0.5 for oblate clusters and 1 for prolate clusters. Both indicators are calculated considering only the metal atoms and excluding the oxygen atoms. Additionally, explicit results are shown only for $Mg_{20}O_m$ and $Zn_{20}O_m$ limits as all the nanoalloys present an intermediate behavior between these limits. One can notice that all clusters experience a similar global volume expansion upon oxidation, that increases as more and more oxygen atoms are added to the system. Metal clusters are known to become more reactive when expanded [45], so the results in Fig. 5 provide an explanation for the accelerated oxidation rate detected in Fig. 3. The global expansion is somehow expected for Zn, because oxidation induces a significant expansion of metal-metal bonds in the local region around oxygen atoms, but it is more strange in Mg because in this case the oxidized region locally shrinks. An additional conclusion from Fig. 5 is that, while the pure clusters are very spherical at the quadrupolar level, oxidation induces a shape deformation away from sphericity, which is more marked in Mg-rich systems. This last observation apparently confirms that Mg-based materials undergo a more significant reconstruction upon oxidation, although we emphasize that Fig. 5 only quantifies the *global* geometrical response of the whole metallic skeleton: by including all metal atoms, it misses relevant local information regarding the different structural response of the oxidized and metallic parts of the cluster.

In order to obtain a more detailed picture of the structural distortions induced by oxidation, we have partitioned the whole set of metal atoms into two subsets: the first subset contains all metal atoms not directly bonded to an oxygen atom. We call d_0 the average metal-metal distance within this subset, which is representative of the "metallic" part of the cluster; the second subset contains all metal atoms bonded to oxygen atoms, so it is representative of the metal oxide phase. Within this second subset, we further differentiate between metal-metal bonds linked to a single oxygen atom (whose average distance is called d_1), and metal-metal bonds linked to two oxygen atoms (whose average distance is called d_2). Notice that each metal-metal bond separates two neighboring hollow sites, so this classification is exhaustive, i.e. there are no metal-metal bonds with more than two oxygen atoms attached. Finally, we define d_{int} as the average length of the bonds formed between a metal atom in the first subset and a metal atom in the second subset. This distance is representative of the metal-oxide interface. These distances are plotted in Fig. 6 for $Mg_{20}O_m$ and $Zn_{20}O_m$ clusters, as a function of
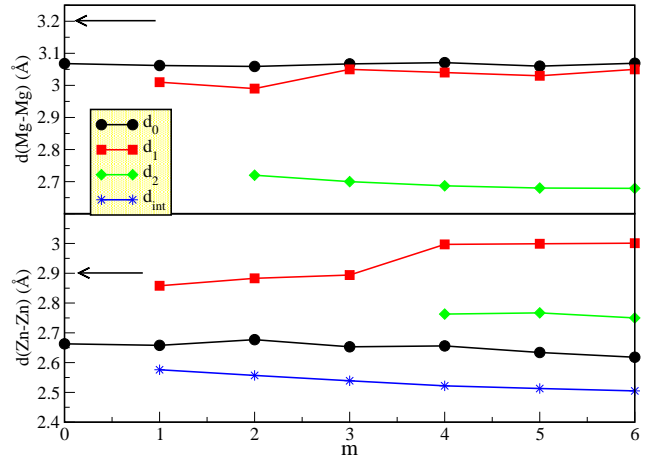
Table 1 Number of Zn-O and Mg-O bonds in $Zn_xMg_{20-x}O_m$. The first number is for Mg-O the second for Zn-O

x/m	1	2	3	4	5	6
20	–/3	–/6	–/9	–/12	–/15	–/18
17	1/2	2/4	3/6	4/8	5/10	6/12
15	2/1	4/2	5/4	6/6	8/7	9/9
13	2/1	4/2	6/3	8/4	10/5	11/7
10	2/1	4/2	6/3	9/4	11/4	14/4
0	3/–	7/–	10/–	13/–	17/–	20/–
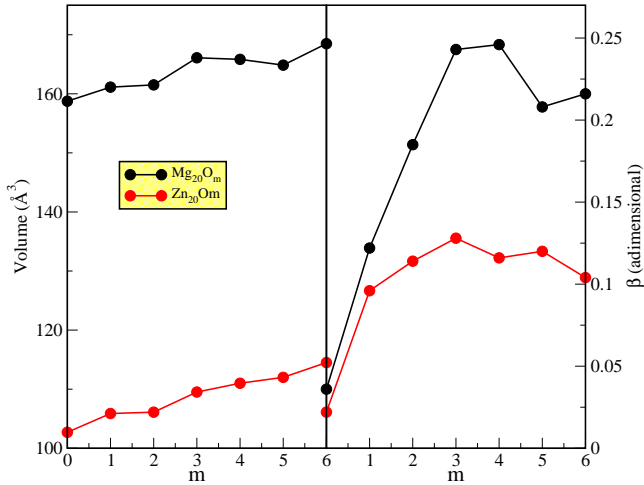
Fig. 5 The volume of the inertia ellipsoid (left panel) and the asphericity parameter β (right panel) are displayed as a function of the oxygen content.

Fig. 6 Locally averaged Mg-Mg distances in $Mg_{20}O_m$ (upper graph) and Zn-Zn distances in $Zn_{20}O_m$ (lower graph) are shown as a function of the oxygen content. d_0 refers to metal-metal bonds in the non-oxidized (metallic) part of the cluster, d_1 and d_2 to the same bonds but in the oxidized region of the cluster; finally d_{int} are the metal-metal distances at the metal-oxide interface. See the main text for more details. d_0 values in the bulk limit are also shown (black arrows), to appreciate the degree of bond length contraction at the nanoscale.

the total oxygen content. As happened with the previous figure, the nanoalloys display an intermediate behavior between these figures, so it is enough with displaying the pure limits to get the whole qualitative picture.

A simple visual inspection of Fig. 6 already demonstrates that Mg and Zn substrates respond in different ways to the oxidation process, mostly due to the different size mismatch at the metal-oxide interface, although there are also some similarities between both systems. In order to attain equally optimal lengths for the stronger metal-oxygen bonds, Mg-Mg bonds slightly contract when put in contact with a single oxygen atom (see d_1 results as a red line), while Zn-Zn bonds significantly expand. Therefore, addition of a single oxygen atom induces a stronger stress on the Zn skeleton compared to the Mg skeleton. However, for both systems d_2 is significantly shorter than d_1, and this has interesting consequences: as more oxygen atoms are added to the system, the oxidation process accumulates a growing tensile stress in the Mg skeleton (as d_2 distances are very much contracted as compared to d_0 distances in Mg); meanwhile, for the Zn cluster, the same oxidation process gradually releases most of the compressive stress initially incurred (as d_2 is only slightly longer than d_0 for the Zn substrate). In fact, it is interesting to notice that d_1 values (around 3Å) and d_2 values (around 2.7Å) are similar in both substrates, demonstrating that it is the metal that structurally adapts to provide the optimal environment to the oxygen atoms. To summarize, the oxidation induces a growing tensile

stress in the Mg substrate, a cumulative effect of an "exploding" nature; while it induces a compressive stress in the Zn substrate, which has a "self-healing" nature. Obviously, the Zn scenario is more appealing for the goal of keeping the metal shell intact while the oxide crust is growing, thus protecting the core.

It is also very interesting that both systems behave similarly concerning their metallic part. In effect, the bond distances in the metallic part of the clusters (d_0) are hardly affected by the oxidation process. The metal and oxide phases seem to be quite independent from each other in their coexistence, and the metal does not significantly respond to the imposed stress, irrespective of its tensile or compressive nature. Therefore, it must be the metal-oxide interface that concentrates the whole of the strain response, and we have observed that this response is also of a very different nature in Mg/MgO and Zn/ZnO interfaces. For $Zn_{20}O_m$ clusters, Fig. 6 shows that interfacial Zn-Zn bonds (d_{int}) are compressed, and by a similar amount to the expansion observed in d_2. The elastic deformation energy is thus dominantly stored in the interfacial bonds, which retain their integrity and sustain the local expansion of the substrate in the oxide phase. On the contrary, the Mg/MgO interface is not able to sustain the much bigger tensile stress induced by oxidation, and it does not retain its

integrity, i.e. we have checked that several Mg-Mg bonds are broken (or dissociated) in the interfacial region after addition of each oxygen atom. The surviving bonds keep a short d_{int} length, and this is why we have decided not to plot them in Fig. 6, as they are not representative of the observed phenomenon. The cluster volume expands (as shown in Fig. 5) even if all the bond lengths contract, simply because the structure becomes less compact because of a reduced number of Mg-Mg bonds. It is indeed expected that bond breaking (which generates some of the open square or pentagonal rings close to the interfacial region) is a mechanism that can alleviate a sufficiently strong tensile stress by creating structural defects in the substrate. This detailed picture confirms that Mg-rich substrates are much more disrupted by the oxidation process, and so are less capable of properly protecting the core against oxygen attack.

It is now easy to understand why Zn-rich nanoalloys are optimal for corrosion applications. In effect, the presence of Mg is beneficial because of its higher reactivity with oxygen, but only in small amounts as we have just demonstrated why Mg-rich materials are deleterious for corrosion protection. The $Zn_{17}Mg_3$ cluster shows optimal properties in this study: first, it has no Mg-Mg bonds which are the most disruptive ones when two oxygen atoms are attached to them; second, it has an average metal-metal bond length slightly longer than in pure Zn_{20}, so the compressive stress at the interface will be even smaller than in pure Zn; moreover, oxygen atoms are initially guided towards Zn-Mg bonds, which are locally slightly longer (2.75-2.80Å) than Zn-Zn bonds, so that oxygen attaches to Zn-Mg bonds at almost zero induced stress cost. In summary, there is an optimal synergy that increases the reactivity while reducing the induced stress at the same time.

The metal-metal shortest interatomic distances in the bulk limit are also shown in Fig. 6. Both metals crystallize in an hcp structure, with d_0 values of (rounded off to the first decimal digit) 2.9Å for Zn and 3.2Å for Mg. As expected, these are both longer than in the small clusters considered in this work. The most important comment is that employment of the bulk d_0 values (instead of the cluster ones) would not fundamentally alter the main conclusions of the paper, although it is interesting to observe that the purely steric factors are size dependent, as they depend of the specific d_0 reference values. If we make the sensible *assumption* that the optimal metal-oxygen bond lengths are roughly size-independent (this is in fact expected as the metal-oxygen interaction is the strongest one in these systems), we can use our results to further discuss the expected size effect on corrosion protection properties. With a longer d_0, bulk Mg would sustain even a stronger tensile stress upon oxidation than Mg nanoparticles do, i.e. bulk Mg would be expected to be even worse than nanoscale Mg for corrosion protecting applications. Meanwhile, bulk Zn would remain approximately at the same quantitative stress level than our studied nanoparticle, but the stress would have a different sign: it would be slightly tensile in the bulk crystal, as opposed to slightly compressive in Zn_{20}. This reasoning suggests that the cluster size is an important extra parameter to fine-tune the corrosion protection properties of nanoparticles, as expected indeed of any cluster study where *size does matter*. Pure Zn nanoparticles of bigger size than here studied, and with $d_0 \approx 2.75$Å will undergo no distortion

upon oxidation, as for them $d_0 \approx d_2$. This would also happen for Zn-rich Zn-Mg nanoalloys at some optimal size.

3.2 Analysis of electronic properties

Now that we have exhausted the purely structural analysis, let's consider what else can be learnt about the corrosion protecting features from the analysis of electronic indicators. What makes Mg and Zn clusters so different, and what makes a certain composition of those elements particularly suitable in the context of optimal coating properties as regards the formation of the surface oxide? It is the aim of the following discussion to provide hints at possible answers for these questions.

Fig. 7 displays the atom condensed Fukui function f^- averaged over all the atoms of each chemical element and discriminating the central (or core) atom from the surface atoms. Several striking features are evident at first sight. The Fukui function of oxygen atoms is smaller than that of Zn and Mg surface atoms, and of the same order as that of the core atom. This means that, in principle, an attacking oxygen atom should not sit in the vicinity of an already adsorbed oxygen atom. In effect, we do not observe any O-O bond, although oxygen atoms can sit relatively close to each other, for example when on the surface of the pure Mg cluster. Obviously, the Fukui function can not anticipate the structure relaxation that occurs after oxygen adsorption as it is an indicator calculated on the fixed geometry of the cluster *before* the oxygen atom is adsorbed, and this is why it was used just to provide some guide but not to completely determine the structural search. Coming back to the central atom, the very weak reported f^- values indicate that upon electron capture, only a very slight change of the charge takes place at the core atom; the charge variation occurs mainly at the surface of the oxidized or non oxidized clusters. The central atom is expected to be the least reactive atom. This is quite noteworthy in the case of the $Zn_{17}Mg_3$ nanoalloy. In fact, whatever the oxygen content, the electrophilic f^- Fukui function of the central atom lies below the f^- of the oxygen atoms for this sole stoichiometry (middle right panel of Fig. 7). Finally, this figure shows that the behavior of the electrophilic f^- Fukui functions of the Zn and Mg surface atoms is at odds. Indeed, for $x = 10, 13, 15$ and 17, the f^- of Zn atoms is almost constant while the f^- of Mg are either decreasing or presenting a descending oscillation. This last trend underlines the effect of the progressive oxidation, that affects more the Mg atoms environment.

Fig. 8 displays, in its top part, the positions of the BCPs with respect to the atomic sites for both the bare nanoalloy with $x = 17$, and the same nanoalloy with the maximum number of O atoms attached. The BCPs, plotted as small green balls identify the different bonds. In all the composition range Zn-Zn, Mg-Mg, Zn-Mg, Zn-O and Mg-O bonds are detected. All these bonds can be classified according to a scheme proposed by Matta[32] and their average values (for all the composition range) are listed in Table 2. Zn-O bonds have a ρ_b value that amounts to 0.09 a.u., with a positive Laplacian and a ratio of the potential energy to the kinetic energy close to 1.0; H_b is also small and negative. All these features point towards a dative bond, a special kind of two-center, two-electron ionocovalent bond where the two shared
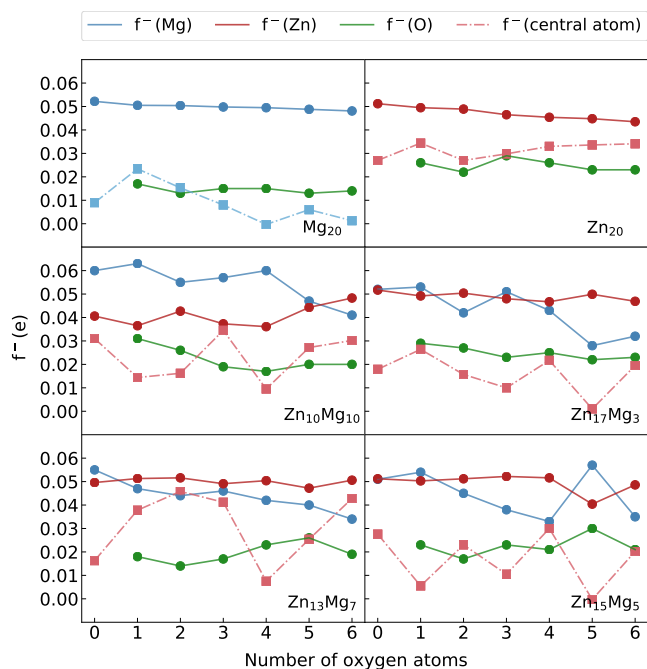
Fig. 7 Atom condensed f^- Fukui functions of $Zn_xMg_{20-x}O_m$ nanoalloys. Blue, red and green circles stand for the average value of f^- for Mg, Zn and O surface atoms, respectively. f^- values for the central atom is also sketched as square symbols.

Fig. 8 BCPs and ELF isosurfaces for selected structures of ZnMg nanoalloys. The top part displays the BCPs as small light green balls whereas Zn, Mg and O atoms are shown with grey, dark green and red balls, respectively. Middle and low panels illustrate the ELF isosurface at ELF=0.8 for both the pure Mg and Zn clusters, and the same clusters oxidized with 6 O atoms. Gray, pink and blue isosurfaces stand for polysynaptic, monosynaptic and core basins, respectively. The small red spheres in the ELF are the oxygen atoms.

electrons are mainly contributed by one of the atoms, Zn in this case. The Mg-O bonds ($\rho_b \approx 0.05$ a.u) have many features in common with the Zn-O bonds, except for a positive H_b, which characterizes this bond as ionic. The bottom panels of Fig. 8 display a representative ELF isosurface (at $\eta = 0.8$) for the $Zn_{20}O_6$ and $Mg_{20}O_6$ clusters. The different nature of Zn-O and Mg-O bonds is also appreciated in the ELF scalar field. In fact, the absence of V(Mg,O) disynaptic basins is an evidence of the ionic character of the bonding, whereas the presence of V(Zn,O) basins close to the O atoms is typical of a dative bonding interaction. V(Zn,O) basins are detected with a population of about 0.8 electrons of which the analysis of the atomic contribution indicates that 0.7 electrons are contributed by the oxygen atom. This last number is in agreement with the traditional picture of the dative bonds between a transition metal (TM) atom and oxygen, that is described by a σ donation of the TM atom and a π back donation of the oxygen atom. Here the π contribution is due to the oxygen atom and the σ contribution to the TM element. The ionocovalent picture of the bond is then illustrated in Fig. 8 with two gray and pink concentric spheres around the O atoms for the $Zn_{20}O_6$ structure (being the ionic nature of the bonding more intense), while the pure ionic bonding in $Mg_{20}O_6$ is depicted with single pink spheres around the O atoms.

Prior to entering into the details of the Zn-Zn, Mg-Mg and Zn-Mg bonding interactions, we note that their $\rho_b \approx 0.025$ a.u. values are at least twice smaller than in the Zn-O and Mg-O bonds. This observation can be connected to the trends discussed above for the interatomic distances and their evolution throughout the ox-
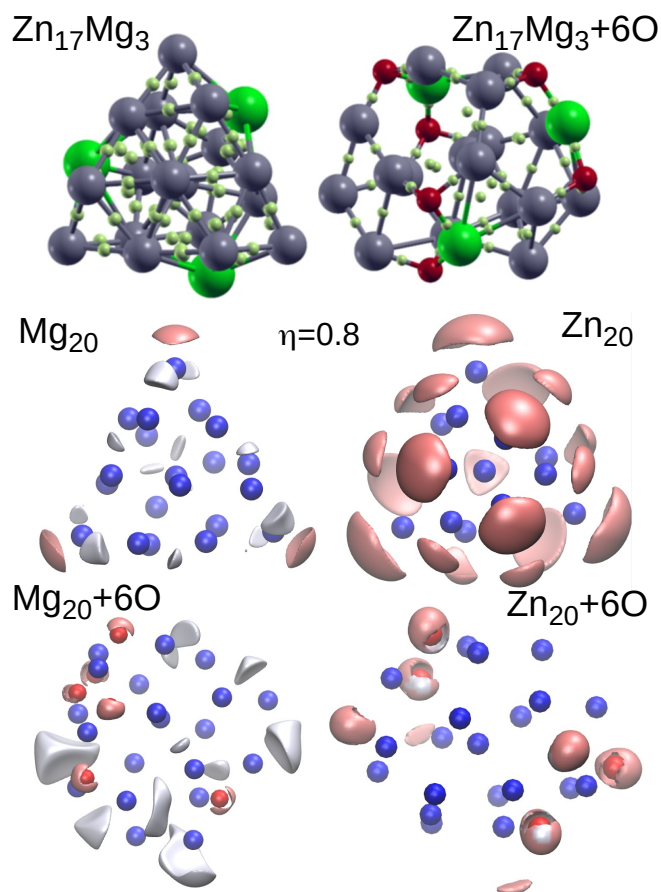
idation process. The Zn-Zn bonds belong to a third category of bonding, the metallic bonding. In fact, small values of ρ_b are obtained and the rest of features also correspond to a metallic bonding, since H_b and $\nabla^2\rho_b$ are slightly negative. The Mg-Mg bonds should be termed as metallic in spite of a negative $\nabla^2\rho_b$ at -0.0006 a.u. It should be noted that very few data for $\nabla^2\rho_b$ are available for bulk metals and they are reported at 0.0002 and -0.0046 a.u. for Na(bcc) and Al(fcc), respectively. The weakness of the Laplacian is assumed to be a signature of metallicity rather than its sign[46].

To better capture the differences in the nature of Mg-Mg and Zn-Zn bonds, the ELF has been plotted also for the bare Mg_{20} and Zn_{20} clusters (middle panels in Fig. 8). Surprisingly, there are no polysynaptic basins in the Zn cluster, whereas almost exactly the opposite happens in the Mg cluster. In fact, for Zn_{20}, the ELF depicts an assembly of monosynaptic basins for every Zn atom, an exception being the central one where all the charge is accumulated in a single core basin. Each monosynaptic valence basin has its attractor located on top of a Zn surface atom at an average

Table 2 Average values of the electronic density, its Laplacian, as well as the energy and the ratio of the potential energy to the kinetic energy at the BCPs for all the composition range. See the section of Computational details for the units. For X-Y bonds with X and Y being Mg or Zn, two values are given. The first one is related to X-Y bonds between two atoms at the surface. The second number is for a X-Y bond between a central atom (X) and a surface atom (Y)

	ρ_b	$\nabla^2\rho_b$	H_b	$\frac{V_b}{G_b}$
Zn-Zn	0.03/0.015	0.08/ 0.03	-0.003/-0.001	1.2/1.0
Mg-Mg	0.02/0.02	-0.006/-0.002	-0.003/-0.003	2.7/2.1
Zn-Mg	0.027/0.026	0.03/ -0.007	-0.006/-0.007	1.4/2.3
Zn-O	0.09	0.4	-0.015	1.1
Mg-O	0.05	0.4	0.01	0.9

distance of 1.9Å. By contrast, for Mg_{20}, polysynaptic basins are mostly observed between pairs of Mg atoms, except for the three apical atoms which sustain monosynaptic basins as well. The data listed in Table 3 show that the electronic population of the core basin associated to the Zn central atom is 30 electrons, which is exactly the electronic population of an isolated Zn atom. This observation suggests that the central Zn atom is isolated from the surface in practical terms. This last point is in line with a previous analysis of the isolation of the core of Zn clusters with respect to their surface[47]. Opposite to this behavior, the Mg central atom is connected to the surface atoms by as many as 5 polysynaptic basins. Turning now our attention to the surface atoms, the ELF of the Mg clusters exhibits di- and trisynaptic valence basins, with electronic populations comprised between 0.5 and 2.0 electrons and a large variance of the populations that ranges between 0.4 and 1.4 electrons, suggesting a high degree of electron delocalization. By comparison, an average value of 2.0 electrons is computed in the V(Zn) monosynaptic basins with an average population variance of 1.4 electrons. Hence, for both pure clusters, a large variance is reported for the valence basin populations; additionally, in Zn_{20}, each monosynaptic valence basin shares a boundary with the monosynaptic valence basins of neighboring Zn atoms, thus forming a connectivity network that percolates the whole cluster surface pointing to a high degree of electron delocalization. Therefore, both Zn_{20} and Mg_{20} have a metallic character at their surface but with a marked difference in the nature of that metallicity, as the electron localization attractors are located at very different positions. The exotic type of metallicity observed in Zn clusters can be ascribed to its peculiar $sp-$hybridization pattern, that was analyzed in a previous work[47]: there, we observed that the $4p-$orbital pointing along the radial direction was completely unoccupied for each surface atom, producing something similar to a sp^2 hybridization mechanism along the directions tangential to the cluster surface. The delocalization associated with this hybridization occurs exclusively along this tangential direction, explaining why the monosynaptic valence basins of the ELF field are only tangentially connected and why the localization attractors occur along the radial direction. Finally, the characterization of the Zn-Mg bond must be addressed; at the surface it resembles that of the Zn-Zn metallic bond, whereas for a Zn central atom connected to a surface Mg atom, the bond is like the Mg-Mg metallic bond. The data reported in the column $\nabla^2\rho_b$ of Table 2 confirms the above assessments.

Having discussed the nature of the reported bonds, it is valuable to investigate how the bonding around the central atom depends on the composition of the nanoalloy. In fact, a good protective layer should isolate the core from the surface, and one expects that the best coating conditions are met when the interactions between the surface and the core regions are kept minimal even after the corrosion process has started. In this respect, Table 3 is not only interesting as far as the two pure metals are concerned. As soon as a small amount of Mg is added to a Zn cluster ($x = 17$), the core basin population of the central atom drops rapidly but without implying connections to the surface of the cluster since no polysynaptic basins are identified involving the central atom. The addition of more Mg atoms ($x = 10, 13, 15$) results in a stronger interaction between the central atom and the surface, but it is mainly an interaction of the central Zn atom with other Zn atoms. Note that the interaction of the central Zn atom with Mg atom at the surface is kept at a low value with even cancellation for the $x = 13$ composition. This feature reinforces the fact that $x = 17$ and $x = 13$ stoichiometries, close to the Mg_2Zn_{11} and $MgZn_2$ compositions, are the best candidates to optimize the protection against corrosion in Zn-Mg alloys, in agreement with the experimental observations.

In addition to the previous analysis, the bare Zn_xMg_{20-x} and the 6 O atoms loaded nanoalloys have been analyzed within the framework of QTAIM. The data are summarized in Table 4. Let us start the analysis with the Mg_{20} cluster. The central Mg atom interacts with the Mg surface atoms exactly in the same manner as two Mg atoms at the surface do (see line Mg-Mg in Table 2). The oxidation with 6 O atoms on the surface gives way to an increase of interaction of the Mg central atom with the Mg surface atoms for the $x = 0$ (Mg_{20}) stoichiometry. In contrast, for the pure Zn stoichiometry, and if the standard deviation is included, the ρ_b values remains roughly constant despite oxidation. Overall, the interaction drops between the central and the surface atoms, however the large standard deviation after 6 O atoms oxidation suggests that locally there is a connection to the surface of the cluster. Two noticeable trends are observed in Zn-rich nanoalloys. For the $x = 13$ stoichiometry, the Zn-Zn core-shell interaction falls down but the single Zn-Mg interaction increases. For the $x = 17$ stoichiometry, both the Zn-Zn and Zn-Mg core-shell interactions drop. Interestingly, the higher degree of isolation of the core from the surface takes place for $x = 13$ and $x = 17$. The $x = 17$ stoichiometry was found above to be characterized by the lowest f^- Fukui function on the central atom. There is an overall agreement between the data provided by the different geometrical and electronic descriptors throughout this work. This supports the idea that nanoalloys close in composition to Mg_2Zn_{11} have optimal properties to act as protective coating. Finally, it is worth stating that for all the 42 structures investigated, no direct interaction between the central atom and an oxygen atom has been found. In fact, neither a BCP nor a disynaptic basin of the ELF appears between the central atom and an attacking O atom.

4 Conclusions

We conducted a comprehensive *ab-initio* study of the initial oxidation stages in Zn_xMg_{20-x} nanoalloys with different compositions

Table 3 Number (N) and populations (Pop) of ELF basins for the Zn_xMg_{20-x} nanoalloys. X_C denotes the central atom, and X_A and X_B other atoms. Populations are given as a number of electrons. In parenthesis, we show the population of a disynaptic valence basin involving the X_C atom and a Mg surface atom

	Mg_{20}	Zn_{20}	$Zn_{17}Mg_3$	$Zn_{15}Mg_5$	$Zn_{13}Mg_7$	$Zn_{10}Mg_{10}$
$N(V(X))$	3	19	16	13	11	8
$N(V(X_A, X_B))$	36	0	21	27	35	36
$N(V(X_C, X_{A/B}))$	5	0	0	16	9	8
$Pop(C(X_C))$	10.0	30.0	27.7	27.8	27.6	27.6
$Pop(\sum V(X_C, ...))$	(3.78)	0	0	7.92(0.68)	9.68(0.00)	12.25(0.76)

Table 4 Average value of the electronic density at the BCPs connecting the central atom to surface atoms. First two rows are for the bare cluster, and last two for the oxidized nanoalloys with 6 oxygen atoms. Within the set of two rows, the first row corresponds to the connection to a surface Zn atom and the second one to the connection with a Mg surface atom Standard deviations are given in parenthesis when more than one value was available

Zn_xMg_{20-x} central atom	x=20 Zn	x=17 Zn	x=15 Zn	x=13 Zn	x=10 Zn	x=0 Mg
ρ_b pristine	0.024(3)	0.024(3) 0.0253(1)	0.026(3) 0.0209(5)	0.027(1) 0.0198	0.025(2) 0.0200	0.0154(2)
ρ_b 6 O atoms	0.019(7)	0.015(2) 0.0134	0.023(5) 0.0261	0.019(4) 0.0217	0.022(3) 0.020(1)	0.0179(4)

($x = 0, 10, 13, 15, 17, 20$), with the goal of understanding why the Zn-Mg mixtures in the Zn-rich side of the phase diagram are optimal as anticorrosive coatings. We focused on the formation of the sacrificial surface oxide layer, which constitutes the first step in the corrosion process, and whose characteristics will condition the next stages. These nanoalloys are model systems to simulate the local environments and related complex processes that occur in extended granular surface coatings.

The results were analyzed from different perspectives, including structural, energetic and electronic indicators, which allowed us to characterize: (a) the local atomic and chemical environments, both in a local neighborhood around the oxygen attack site and in the oxygen-free metallic part; (b) the subtle interplay between the selective reactivity of different parts of the system and the resulting structural rearrangements induced by oxidation, with particular interest in the degree of protection of the core region provided by the oxygen crust; and (c) the different bonding patterns and how they reveal an electronic redistribution that might be optimal in certain cases for protecting the core from the attack of other radicals in the presence of the already formed surface oxide crust.

We found that oxygen adsorption becomes a more exothermic process the larger the oxygen content, so that the oxide phase grows at an accelerated rate at least during its initial growth stage. At low Mg concentrations, Mg atoms occupy well separated and highly-coordinated surface sites. In the initial stages of oxidation, those Mg atoms in the shell act as attractors that anchor the oxygen adatoms, creating several nucleation centers evenly distributed across the cluster surface. The Mg atoms guide the oxygen atoms precisely towards those local regions in the surface that contain the strongest Zn-Mg metallic bonds, which are the most resistant ones at a structural level, as a consequence of which Mg atoms also protect surface defects from being attacked by oxygen in the initial stages of oxidation. All these properties conspire precisely to promote the growth of the oxide crust whilst protecting the core, an example of a very positive synergy between Zn and Mg for this particular application.

As metal-oxide bonds are approximately 5 times stiffer than metal-metal bonds, it is mainly the metallic region close to the metal-oxide interface the one that deforms in response to the stress incurred upon oxidation. The $Zn_{17}Mg_3$ composition shows optimal properties in this study: first, it has no Mg-Mg bonds which are the most disruptive ones upon oxygen adsorption; second, it has an average metal-metal bond length optimal to minimize the compressive stress at the interface between the oxidized part and the metallic part of the system; moreover, oxygen atoms are initially guided towards Zn-Mg bonds at almost zero induced stress cost. We have also discussed the expected cluster size dependence of the induced local deformation and stress, suggesting that there exist optimal sizes for which the induced stress is minimal.

The electronic indicators show that as soon as a small amount of Mg is added to a Zn cluster, the atom at the core becomes the least reactive atom in the system and is disconnected from the surface in practical terms. Further addition of Mg within the Zn-rich side of the phase diagram results in a stronger interaction between the central atom and the surface, but it is mainly an interaction of the central Zn atom with other Zn atoms while the interaction of the central Zn atom with Mg atoms at the surface remains very weak. These features reinforce the conclusion that $x = 17$ and $x = 13$ stoichiometries, close to the Mg_2Zn_{11} and $MgZn_2$ compositions respectively, are the best candidates to optimize the protection against corrosion in Zn-Mg alloys, in agreement with the experimental observations. We strongly believe that our results will serve to better guide the design of specific protective coatings based on Zn and Mg. The present work could be extended along several lines. One of them would be to consider larger nanoalloys with a bigger core, and to analyze the structural and electronic properties of the fully oxidized crust. Further studies should also focus on the response of the oxidized Zn-Mg nanoalloys to the attack of chloride ions, of prime importance to understand the resistance to corrosion in an oceanic atmosphere, but also quite relevant in the domain of biomedical materials where Zn-Mg alloys are used to manufacture orthopedic

prosthesis. These lines will be pursued in our long-term project devoted to unveiling the fundamental aspects that trigger the optimal anticorrosive properties of Zn-Mg coatings.

Conflicts of interest

There are no conflicts to declare.

Acknowledgements

Notes and references

1 F. Thébault, B. Vuillemin, R. Oltra, C. Allely, K. Ogle and O. Heintz, *Corros. Sci.*, 2015, **97**, 100–106.

2 N. Hosking, M. Ström, P. Shipway and C. Rudd, *Corros. Sci.*, 2007, **49**, 3669–3695.

3 A. I. Ikeuba, F. Kou, H. Duan, B. Zhang, J. Wang, E.-H. Han and W. Ke, *J. of Solid State Electrochem.*, 2019, **23**, 1165–1177.

4 T. Prosek, A. Nazarov, U. Bexell, D. Thierry and J. Serak, *Corros. Sci.*, 2008, **50**, 2216–2231.

5 S. Sabooni, M. Ahmadi, E. Galinmoghaddam, R. Westerwaal, C. Boelsma, E. Zoestbergen, G. Song and Y. T. Pei, *Materials & Design*, 2020, **190**, 108560.

6 T. A. Vida, T. Soares, R. S. Septimio, C. C. Brito, N. Cheung and A. Garcia, *Mat. Res.*, 2019, **22**, 1–13.

7 M. Ropo, M. Punkkinen, P. Kuopanportti, M. Yasir, S. Granroth, A. Kuronen and K. Kokko, *Sci. Rep.*, 2021, **11**, 1–13.

8 E. Diler, S. Rioual, B. Lescop, D. Thierry and B. Rouvellou, *Corros. Sci.*, 2012, **65**, 178–186.

9 E. Diler, B. Lescop, S. Rioual, G. N. Vien, D. Thierry and B. Rouvellou, *Corros. Sci.*, 2014, **79**, 83–88.

10 S. Shen and Y. Zuo, *Corros. Sci.*, 2014, **87**, 167–178.

11 A. Lebon, A. Aguado and A. Vega, *Corros. Sci.*, 2017, **124**, 35–45.

12 P. Álvarez-Zapatero, A. Vega and A. Aguado, *Nanoscale*, 2020, **12**, 20432–20448.

13 P. Álvarez Zapatero, A. Vega and A. Aguado, *Acta Materialia*, 2021, **220**, 117341.

14 C. D. Taylor, *Int. J. Corros.*, 2012, **2012**, 1–13.

15 Y. Jin, M. Liu, C. Zhang, C. Leygraf, L. Wen and J. Pan, *J. Elec. Soc.*, 2017, **164**, C465.

16 C. Örnek, M. Liu, J. Pan, Y. Jin and C. Leygraf, *Topics in Cat.*, 2018, **61**, 1169–1182.

17 G. Kresse and J. Hafner, *Phys. Rev. B*, 1993, **47**, 558.

18 G. Kresse and J. Furthmüller, *Phys. Rev. B*, 1996, **54**, 11169.

19 J. P. Perdew, K. Burke and M. Ernzerhof, *Phys. Rev. Lett.*, 1996, **77**, 3865.

20 J. E. Jaffe, J. A. Snyder, Z. Lin and A. C. Hess, *Phys. Rev. B*, 2000, **62**, 1660.

21 B. Meyer and D. Marx, *Phys. Rev. B*, 2003, **67**, 035403.

22 Ü. Özgür, Y. I. Alivov, C. Liu, A. Teke, M. A. Reshchikov, S. Doğan, V. Avrutin, S.-J. Cho and H. Morkoç, *J. App. Phys.*, 2005, **98**, 11.

23 R. Bader, *Atoms in Molecules: A Quantum Theory*, Clarendon Press, 1990.

24 G. Henkelman, A. Arnaldsson and H. Jónsson, *Comput. Mater. Sci.*, 2006, **36**, 354–360.

25 P. Fuentealba, P. Pérez and R. Contreras, *J. Chem. Phys.*, 2000, **113**, 2544–2551.

26 W. Yang and R. G. Parr, *Proc. Natl. Acad. Sci. U.S.A.*, 1985, **82**, 6723–6726.

27 P. Geerlings, F. De Proft and W. Langenaeker, *Chem. Rev.*, 2003, **103**, 1793–1874.

28 A. D. Becke and K. E. Edgecombe, *J. Chem. Phys.*, 1990, **92**, 5397–5403.

29 P. P. L., *Atoms in Molecules: an Introduction*, Prentice Hall, 1999.

30 R. F. Bader and C. F. Matta, *Inorg. Chem.*, 2001, **40**, 5603–5611.

31 R. F. Bader, C. F. Matta and F. Cortés-Guzmán, *Organometallics*, 2004, **23**, 6253–6263.

32 C. F. Matta, in *Hydrogen–Hydrogen Bonding: The Non-Electrostatic Limit of Closed-Shell Interaction Between Two Hydro*, ed. S. J. Grabowski, Springer Netherlands, Dordrecht, 2006, pp. 337–375.

33 B. Silvi and A. Savin, *Nature*, 1994, **371**, 683–686.

34 M. J. Frisch, G. W. Trucks, H. B. Schlegel, G. E. Scuseria, M. A. Robb, J. R. Cheeseman, G. Scalmani, V. Barone, G. A. Petersson, H. Nakatsuji, X. Li, M. Caricato, A. V. Marenich, J. Bloino, B. G. Janesko, R. Gomperts, B. Mennucci, H. P. Hratchian, J. V. Ortiz, A. F. Izmaylov, J. L. Sonnenberg, D. Williams-Young, F. Ding, F. Lipparini, F. Egidi, J. Goings, B. Peng, A. Petrone, T. Henderson, D. Ranasinghe, V. G. Zakrzewski, J. Gao, N. Rega, G. Zheng, W. Liang, M. Hada, M. Ehara, K. Toyota, R. Fukuda, J. Hasegawa, M. Ishida, T. Nakajima, Y. Honda, O. Kitao, H. Nakai, T. Vreven, K. Throssell, J. A. Montgomery, Jr., J. E. Peralta, F. Ogliaro, M. J. Bearpark, J. J. Heyd, E. N. Brothers, K. N. Kudin, V. N. Staroverov, T. A. Keith, R. Kobayashi, J. Normand, K. Raghavachari, A. P. Rendell, J. C. Burant, S. S. Iyengar, J. Tomasi, M. Cossi, J. M. Millam, M. Klene, C. Adamo, R. Cammi, J. W. Ochterski, R. L. Martin, K. Morokuma, O. Farkas, J. B. Foresman and D. J. Fox, *Gaussian 16 Revision C.01*, 2016, Gaussian Inc. Wallingford CT.

35 A. Otero-de-la Roza, E. R. Johnson and V. Luaña, *Computer Phys. Comm.*, 2014, **185**, 1007–1018.

36 S. Noury, X. Krokidis, F. Fuster and B. Silvi, *Comp. & Chem.*, 1999, **23**, 597–604.

37 M. Kohout, *DGrid, version 5.1, Dresden*, 2019, https://www2.cpfs.mpg.de/~kohout/Documents/dgrid-html/dgrid.html.

38 G. Henkelman, B. P. Uberuaga and H. Jónsson, *J. Chem. Phys.*, 2000, **113**, 9901–9904.

39 G. Henkelman and H. Jónsson, *J. Chem. Phys.*, 2000, **113**, 9978–9985.

40 C. Hock, S. Strassburg, H. Haberland, B. v. Issendorff, A. Aguado and M. Schmidt, *Phys. Rev. Lett.*, 2008, **101**, 023401.

41 K. Majer, M. Lei, C. Hock, B. von Issendorff and A. Aguado, *J. Chem. Phys.*, 2009, **131**, 204313.

42 H. S. H. U. Borgstedt and G. Wittig, *Atomwirtschaft-Atomtechnik*, 1972, **17**, 157.

43 D. L. Hill and J. A. Wheeler, *Physical Review*, 1953, **89**, 1102.

44 W. A. De Heer, *Rev. Mod. Phys*, 1993, **65**, 611.

45 B. Cao, A. K. Starace, O. H. Judd, I. Bhattacharyya, M. F. Jarrold, J. M. López and A. Aguado, *J. Am. Chem. Soc.*, 2010, **132**, 12906–12918.

46 B. Silvi, R. Gillespie and C. Gatti, in *Electron Density Analysis*, ed. J. Reedijk and K. Poeppelmeier, Elsevier, Oxford, 2013, pp. 187–226.

47 A. Aguado, A. Vega, A. Lebon and B. von Issendorff, *Angew. Chem. Int. Ed.*, 2015, **54**, 2111–2115.